CO$_2$ hydrogenation to methanol over Cu catalysts supported on La-modified SBA-15: The crucial role of Cu–LaO$_x$ interfaces

Kun Chen[a], Huihuang Fang[a], Simson Wu[b], Xi Liu[c], Jianwei Zheng[b], Song Zhou[d], Xinping Duan[a], Yichao Zhuang[a], Shik Chi Edman Tsang[b], Youzhu Yuan[a],*

[a] State Key Laboratory of Physical Chemistry of Solid Surfaces, iChEM, National Engineering Laboratory for Green Chemical Productions of Alcohols–Ethers–Esters, College of Chemistry and Chemical Engineering, Xiamen University, Xiamen, 361005, China
[b] Wolfson Catalysis Centre, Department of Chemistry, University of Oxford, Oxford, OX1 3QR, UK
[c] Syncat@Beijing, Synfuels China. Co. Ltd, State Key Laboratory of Coal Conversion, Institute of Coal Chemistry, Chinese Academy of Sciences, Beijing, 101407, China
[d] State Key Laboratory of Coal Conversion, Institute of Coal Chemistry, Chinese Academy of Sciences, Beijing, 101407, China

ARTICLE INFO

ABSTRACT

The direct hydrogenation of CO$_2$ to methanol has become a very active research field because CO$_2$ can be prospectively recycled to mitigate greenhouse effect and store clean synthetic fuels. This reaction can be catalyzed by supported Cu catalysts and the catalysts display strong support or promoter effects. Sintering of Cu species accelerates the separation of Cu–oxide interfaces, reduces the active component, and diminishes the methanol selectivity. In this work, we report a Cu catalyst supported on La-modified SBA-15, where the Cu–LaO$_x$ interface is generated through the interaction of highly dispersed Cu nanoparticles with LaO$_x$ species bedded into the SBA-15 pore wall. The optimized Cu$_1$La$_{0.2}$/SBA-15 catalyst can achieve methanol selectivity up to 81.2% with no deterioration in activity over 100 h on stream compared with the La-free catalyst. A thorough study reveals that La species not only significantly improve the CO$_2$ adsorption but also enhance Cu dispersion to produce well-dispersed active sites. The H/D exchange experiments show that the methanol synthesis displays a strong thermodynamic isotope effect and the Cu–LaO$_x$ interface plays a crucial role for the methanol synthesis rate in CO$_2$/D$_2$ feed. In situ DRIFTS studies reveal that *HCOO and *OCH$_3$ species are the key intermediates formed during the activation of CO$_2$ and methanol synthesis over the Cu$_1$La$_{0.2}$/SBA-15 catalyst.

1. Introduction

With alarming reports that link CO$_2$ emissions to global warming and the urgent demand for clean and renewable energy sources, researchers both in academia and industry have put great efforts on developing a new sustainable non-fossil route [1]. Solar, wind, hydraulic, hydrogen, or biomass energies can partially substitute fossil fuels to address the issues of depletion of oil resources and greenhouse gas emissions [2]. Recent progress has revealed that the advances in capture and separation can effectively facilitate large-scale CO$_2$ utilization [3]. Unnatural processes generally convert CO$_2$ into products including urea and polycarbonate plastics, but converting CO$_2$ to valuable chemical raw materials or fuels via a catalytic process is also highly desirable. For example, CO$_2$ reduction using hydrogen from renewable sources (e.g., H$_2$O) is an attractive paradigm to mitigate the environmental problems associated with elevated atmospheric CO$_2$ concentration. This process also provides energy storage from H$_2$ with

improved portability and potential to utilize established infrastructures [4,5].

Methanol is a desirable hydrogen liquid carrier and a key material for the synthesis of high-value chemicals, such as olefins (via the methanol to olefin process), gasoline (via the methanol to gasoline process), biodiesel, and fuel additive [6]. Industrial methanol synthesis from CO$_2$-containing syngas (derived from fossil resources) uses Cu/ZnO/Al$_2$O$_3$ as a catalyst at elevated pressure (50–100 bar) and temperature (200–300 °C). Bulk CuZnO-based catalysts prepared through co-precipitation method can catalyze the formation of methanol from sole CO$_2$ and produce CO as a by-product via reverse water-gas shift (RWGS) reaction [7,8]. Scientists aim to identify the nature of active sites in CuZnO to optimize catalytic efficiency for the selective CO$_2$ hydrogenation to methanol [9,10]. The results point out that the detailed structure of the active catalytic site is likely attributed to the well synergy of Cu and ZnO$_x$ at the interface, which facilitates the methanol synthesis via formate intermediates. In general, an undistorted pure Cu

---

surface is preferred to convert CO_2 to CO, but the combination of Cu and ZnO greatly boosts the methanol synthesis rates [11,12]. However, $Cu–ZnO_x$ interface separation is accelerated during the hydrothermal reaction, thereby reducing the active component and diminishing methanol selectivity [13,14]. This instability drives us to explore the rational design of sufficient active interfaces between metal and oxide for the catalytic conversion of CO_2 to methanol.

Metal–oxide interfaces have been proposed to play a vital role in the reactivity of supported catalysts since each material can provide a distinct functionality that is necessary for efficient catalysis in complex reaction pathways. Several works have been published which study the significance of interfacial sites and how to manipulate it for important reactions such as CO oxidation, steam reforming of methanol, and CO_2 reduction [15–18]. For example, Zhang et al. [19] designed a Pd/SnO_2 catalyst with abundant Pd–O–Sn interfaces to enable multi-electron transfer for selective electroreduction of CO_2 to methanol. Such interfacial effects are encouraging, but the impact could be limited due to the low efficiency. The most promising and well-studied non-precious metal catalysts for CO_2 to methanol are Cu-based catalysts. At present, improving the performance of Cu-based catalysts for CO_2 hydrogenation to methanol is predominantly focused on increasing the dispersion of Cu nanoparticles (NPs) [20], varying the preparation method and/or metal precursor [21,22], and further adding promoters [23]. However, investigations into the application of catalysts with Cu alone are limited, which is likely due to their short stability and low selectivity to methanol. Cu-based catalysts modified with MO_x (M = Ce [24], Mn [24], Y [25], Ga [26], Zr [27], Si [28], Ti [28], and Mg [29]) have promotional effects on catalytic performance because of interfacial effects between the multi-component metal phases. For instance, Graciani et al. [30] revealed that the metal oxide $Cu–CeO_x$ interfaces over $CeO_x/Cu(111)$ and $Cu/CeO_x/TiO_2(110)$ directly activated CO_2 in the form of carboxylate ($CO_2^{\delta-}$) and lead to methanol synthesis rates with considerably faster than those over traditional Cu–ZnO-based catalysts. Additionally, the dispersion of $Cu–MO_x$ active species remarkably influences the catalytic activity [31,32]. As an alternative to the conventional process, Li et al. [33] used a surfactant-assisted co-precipitation method to prepare mesoporous $CuO–ZnO–ZrO_2$ catalysts. They found that the increased turnover frequency (TOF) for the methanol formation was attributed to the dispersion of small Cu particles on mesoporous structures, which maintained the large interfacial area of the $Cu–ZnO_x$ and/or $Cu–ZrO_x$ interfaces.

On the other hand, previous results have proven that the incorporation of basic elements can help the Cu-based catalysts in selective methanol formation [34]. In particular, the basicity of support is expected to increase the adsorption or activation of mildly acidic CO_2. For example, the oxides of basic elements, such as K [35], Ba [35], La [36,37], and Ca [38], have been used as promoters to improve the adsorption strength of CO_2. Notably, La doping on Cu/ZrO_2 promotes formate hydrogenation to methanol and inhibits its dissociation into CO. The apparent activation energy (E_a) for methanol formation declines with increasing La loading, whereas the opposite trend was observed for CO formation [36]. The modified effects of La oxide reportedly originate from several aspects, such as the textural change in catalyst to form basic active sites or to improve the metal surface area [39,40]. A specific form of these promoter effects was prominent in our previous study, where an unusual interaction was locally found on the interfacial area of the $Cu/La_2O_2CO_3$-R catalyst and markedly enhanced the CO_2 activation and methanol synthesis rates over the new type of surface $Cu–LaO_x$ compound [41]. However, the destructive effects of the catalyst structure caused by hydrothermal conditions greatly decrease the catalytic activity. From a structural perspective, dispersed $Cu–MO_x$ on porous materials is expected to simplify the complex catalytic system. By offering high surface areas, good thermal/chemical stability, and pore-size confinement, mesoporous silica materials are ideal hosts to yield a well-dispersed active compound [42,43]. Tada et al. [44] used a simple incipient wetness impregnation method to

deposit $Cu/a-ZrO_2$ ($a-ZrO_2$: amorphous ZrO_2) onto mesoporous silica KIT-6; a highly dispersed Cu species in close contact with $a-ZrO_2$ (partially inverted to $Cu_xZr_yO_z$ after H_2 reduction) was observed to result in better methanol production rate than $Cu/a-ZrO_2$. Such interfacial effects from $Cu–ZrO_x$ or $Cu–ZnO_x$ are typically observed on CO_2 hydrogenation to methanol, however, reports on $Cu–LaO_x$ interface are lack of in-depth study.

Indeed, obtaining stable $Cu–LaO_x$ interface on the lanthanum oxide supports might be difficult and challenging because the strong basicity of supports often results in the easy adsorption of water and CO_2 from air or under reaction conditions. A promising approach is to employ confined growth strategy in which small amount of La oxides are dispersed onto the porous material surface to stabilize and maximize $Cu–LaO_x$ interface. Here, we report a Cu catalyst supported on La-modified SBA-15, where a $Cu–LaO_x$ interface is generated through the interaction of highly dispersed Cu NPs with La species on the SBA-15 surfaces. The optimized $Cu_1La_{0.2}/SBA-15$ catalyst displays considerable methanol selectivity and stability compared with the La-free $Cu_1La_0/SBA-15$ catalyst. The nature and catalytic mechanisms of Cu/La/O nanocomposites in the selective CO_2 hydrogenation to methanol are investigated in detail.

2. Experimental

2.1. Catalyst preparation

Mesoporous SiO_2 (SBA-15) was prepared through the hydrothermal method as reported by Zhao et al. [45]. A series of $Cu_1La_x/SBA-15$ catalysts was prepared by a two-step impregnation method. First, to immobilize La into mesoporous nanochannels, SBA-15 was mixed with a desired amount of lanthanum nitrate ($La(NO_3)_3·6H_2O$, Aladdin, 99.9% purity) solution by ultrasonic treatment for 1 h. The resultant was allowed to stand for 24 h and water was vaporized at 80 °C. Second, Cu catalysts supported on La-modified SBA-15 were prepared by conventional impregnation. The La/Cu atomic ratio was varied from 0 to 0.35, whereas the actual Cu loading was fixed at 10 wt%. The catalyst precursors were air-dried at 80 °C overnight and then calcined at an elevated temperature up to 700 °C for 4 h in an air flow of 100 mL/min. The prepared catalysts were named $Cu_1La_x/SBA-15$ (x = 0, 0.05, 0.1, 0.2, 0.35), where x is the atomic ratio of La to Cu.

2.2. Catalyst characterization

The powder X-ray diffraction (XRD) patterns of the samples were recorded on a Rigaku D/max-RA powder diffractometer (Rigaku, Tokyo, Japan) equipped with a graphite monochromator and Cu-K_α radiation (35 kV and 25 mA). Prior to testing, the samples were pretreated at 300 °C in 5% H_2–95% N_2 for 2 h. The loading of supported metals in the catalysts was measured via inductively coupled plasma atomic emission spectrometry (ICP-AES) on a Thermo IRIS Intrepid II XSP emission spectrometer after diluting metal ions in 5 wt% HCl solution.

Transmission electron microscopy (TEM) images were obtained on a TECNAI F-30 transmission electron microscope operating at an acceleration voltage of 300 kV. Scanning transmission electron microscopy with energy-dispersive spectroscopic (STEM-EDS) elemental mapping of the catalysts was characterized using the same spectrometer operated at 300 kV using a high-angle annular dark-field detector (HAADF) in the STEM mode. Brunauer–Emmett–Teller (BET) surface areas of the catalysts were measured by nitrogen adsorption on a Micromeritics ASAP 2020 at −196 °C (77 K). The H_2-TPR measurements were carried out by the Micromeritics Autochem II ASAP 2920 equipment with a thermal conductivity detector (TCD). First, the catalysts were pretreated at 100 °C for 60 min in a flowing stream of high-purity argon. After cooling to room temperature, a 5% H_2 in N_2 gas mixture (20 mL/min) was introduced, and the temperature was raised from room

temperature to 750 °C at a rate of 10 °C/min. For the as-prepared catalyst samples, CO_2 temperature-programmed desorption ($CO_2 - TPD$) was performed using the same Micromeritics Autochem II ASAP 2920 with TCD. CO_2 chemisorption of the samples was measured by Micromeritics ASAP 2020 with a chemisorption module. Solid-state ^{29}Si magic angle spinning nuclear magnetic resonance spectra (^{29}Si MAS NMR) were obtained using a Bruker Avance III spectrometer. Powder samples (70 mg) were pre-treated overnight at 80 °C under vacuum. ^{29}Si MAS NMR spectra were recorded using a 4 mm MAS probe at a spinning rate of 12 kHz. The Cu surface area and dispersion of the catalysts were determined on a Micromeritics Autochem II 2920 apparatus with a TCD by N_2O chemisorption and H_2 pulse reduction methods based on the stoichiometry of $[2Cu\,(s) + N_2O \rightarrow Cu_2O\,(s) + N_2]$, where Cu (s) represents the surface Cu atom [46]. The measurement steps are described as follows: (1) Samples were reduced in a 5% H_2–95% Ar atmosphere at 300 °C for 2 h and the amount of H_2 consumption denoted as X. (2) The surface reduced Cu was oxidized to Cu^+ by N_2O. (3) The surface Cu_2O was reduced to $Cu°$ by dosing H_2 and the amount of H_2 consumption denoted as Y. Pulse dosing was repeated at an interval of 3 min until the detected TCD peaks for the latest two or more pulses were constant in area. Cu dispersion of all of samples was calculated by Eq. (1). The exposed Cu specific surface area was calculated by Eq. (2).

$$D_{Cu} = \frac{2Y}{X} \times 100\% \tag{1}$$

$$SA_{Cu} = \frac{n_{Cu} \times N}{1.4 \times 10^{19} \times M \times X}\text{(based on Cu metal)} \tag{2}$$

$$n_{Cu} = 2Y \tag{3}$$

Where D_{Cu} (Cu dispersion) is defined as the ratio of exposed Cu on the surface to total Cu; SA_{Cu} is the exposed Cu surface area per gram of Cu metal; W is the weight of the reduced catalyst; M is the relative atomic mass of Cu; n_{Cu} in Eq. (3) is molar number of Cu, N is the Avogadro's constant (6.02×10^{23} atoms mol^{-1}) and 1.4×10^{19} is the number of Cu atoms per square meter.

X-ray absorption spectroscopy (XAS) spectra for all the Cu samples were recorded in transmission mode at the Cu K absorption edge of the B18 XAS beamline at the Diamond Light Source (London, UK). To examine the local structural properties around the Cu atoms, the X-ray absorption fine structure (EXAFS) data were extracted from full XAS spectra. The EXAFS data were analyzed using Athena and Artemis software following a standard procedure. At least three scans were collected to ascertain the reproducibility of the experimental data. The spectra were calibrated with Cu foil as a reference. The amplitude was obtained from EXAFS data analysis of Cu foil. This parameter was used as a fixed input parameter in data fitting to allow refinement in the coordination number of the absorption element. X-ray photoelectron spectroscopy (XPS) and Auger electron spectroscopy (XAES) on Qtac-100 LEIS spectrometer were used for in situ catalyst characterization. Firstly, the catalyst was made into a small disk (4.0 mm diameter) and held on the sample holder. Then, the catalyst was reduced in the pre-treatment chamber at 300 °C for 2 h under 30 mL/min flow of 5% H_2–95% N_2. After cooling down, the sample was introduced into the ultra-high vacuum chamber for XPS measurement at room temperature. Binding energy was calibrated using the C 1s peak at 284.6 eV as a reference. Experimental errors were within ± 0.2 eV. High-sensitivity low-energy ion scattering (HS-LEIS) spectra were also obtained using an IonTOF Qtac100 low-energy ion scattering analyzer. Ne^+ ions with a kinetic energy of 5 keV were applied at a low ion flux of 445 pA/cm^2; they provide good sensitivity for heavy elements (Cu and La) even though they are unsuitable for the measurement of light elements (O and Si). The in situ diffuse reflectance infrared Fourier transform spectroscopy (DRIFTS) of CO_2 hydrogenation was performed using a Nicolet 6700 spectrometer at a special resolution of 2/cm, equipped with a mercury cadmium telluride detector cooled by liquid nitrogen. A Harrick high-pressure reaction cell was fitted with ZnSe windows and

connected to a gas control system. The total flow rate was controlled by a mass flow meter. Prior to the catalytic hydrogenation of CO_2, the catalyst samples were in situ reduced under 5% H_2–95% N_2 at 300 °C for 2 h.

2.3. Catalyst activity evaluation

The catalytic performance of Cu_1La_x/SBA-15 catalysts for CO_2 hydrogenation was tested in continuous flow mode using a stainless-steel fixed-bed tubular reactor equipped with a computer-controlled system. Following pre-treatment, 50 mg catalyst (40–60 mesh) diluted with quartz sand to the fixed bed height was in situ reduced under 30 mL/min flow of 5% H_2–95% N_2 at atmospheric pressure. The reduction temperature was programmed to increase from room temperature to 300 °C at a ramping rate of 2 °C/min and maintained for 2 h. The reaction products were analyzed via online gas chromatography (GC). The composition of the outlet gas was determined using the N_2 internal standard method. The gas concentrations were analyzed through two online GCs respectively equipped with a flame ionization detector for CH_3OH and CH_4 and a TCD for N_2, CO, and CO_2. The reactant flow was held at a constant GHSV of 12,000 mL(STP)/g_{cat}h, $V(H_2):V(CO_2):V(N_2) = 72:24:4$, 240 °C, and 3.0 MPa. The stability tests were performed under the same space velocity and pressure at 240 °C for 100 h.

The conversion of CO_2 (X_{CO2}) was calculated using Eq. (4).

$$X_{CO_2}(\%) = \frac{[CO_2]_{in} - [CO_2]_{out}}{[CO_2]_{in}} \times 100\% \tag{4}$$

where $[CO_2]_{in}$ and $[CO_2]_{out}$ represent the CO_2 concentrations in the inlet and outlet gas, respectively.

CO selectivity (S_{CO}) was calculated using Eq. (5).

$$S_{CO}(\%) = \frac{[CO]_{out}}{[CO_2]_{in} - [CO_2]_{out}} \times 100\% \tag{5}$$

where $[CO]_{out}$ represents the CO concentration in the outlet gas.

Methanol selectivity (S_{CH3OH}) was calculated using Eq. (6).

$$S_{CH_3OH}(\%) = \frac{[CH_3OH]_{out}}{[CH_3OH]_{out} + [CH_4]_{out}} \times (1 - S_{CO}) \times 100\% \tag{6}$$

where $[CH_3OH]_{out}$ represents the CH_3OH concentration in the outlet gas.

TOF was calculated using Eq. (7).

$$\text{TOF (h}^{-1}) = \frac{X_{CO_2} \times [CO_2]_{total}}{m_{catalyst} \times [Cu]_{content} \times D_{Cu} \div M_{Cu}} \tag{7}$$

Where X_{CO_2} is the conversion of CO_2, $[CO_2]_{total}$ is the total capacity of CO_2 (mol/h), $m_{catalyst}$ is the mass of catalyst, $[Cu]_{content}$ is the content of Cu in catalyst based on ICP result, D_{Cu} is the Cu dispersion on catalyst based on N_2O chemisorption, and M_{Cu} is the relative atomic mass (63.55 g/mol).

3. Results and discussion

3.1. Structural characterization of Cu_1La_x/SBA-15

The textural properties of Cu_1La_x/SBA-15 varied with the La content were characterized by using N_2 adsorption–desorption, XRD, N_2O chemisorption–H_2 pulse reduction, and TEM. All N_2 adsorption–desorption isotherms of as-calcined Cu_1La_x/SBA-15 samples are shown in Figure S1. The profiles exhibited typical type VI isotherms with an H1 hysteresis loop, indicating the presence of mesostructures with 1D cylindrical channel. Figure S2 provides the pore size distribution curves. The average pore diameter, total pore volume, and BET specific surface area of each sample are summarized in Table 1. In comparison, the surface area decreased from 676.4 m^2/g for pristine SBA-15 to 324.7 m^2/g for Cu_1La_0/SBA-15, and the total pore volume also decreased from 0.80 cm^3/g to 0.49 cm^3/g. In La-containing

Table 1
Textural property of as-prepared catalysts.

Sample	S_{BET} (m²/g)[a]	V_{pore} (cm³/g)[b]	d_{pore} (nm)[c]	$D_{crystallite}$ (nm)[d]	D_{Cu} (%)[e]	SA_{Cu} (m²/g)[e]	CO₂ uptake (μmol/g)[f]
SBA-15	676.4	0.80	5.4	–	–	–	–
Cu₀La₀.₂/SBA-15	539.6	0.62	5.2	–	–	–	162.8
Cu₁La₀/SBA-15	324.7	0.49	4.8	15.2	11.8	38.2	36.1
Cu₁La₀.₀₅/SBA-15	466.6	0.55	5.0	10.3	13.6	44.2	54.7
Cu₁La₀.₁/SBA-15	475.3	0.59	5.2	6.1	16.4	53.4	72.9
Cu₁La₀.₂/SBA-15	470.3	0.58	5.3	3.8	23.5	76.4	152.5
Cu₁La₀.₃₅/SBA-15	347.6	0.52	4.9	5.7	19.0	61.8	160.4

[a] BET specific surface area.
[b] Total pore volume estimated at $P/P_0 = 0.99$.
[c] BJH pore diameter estimated from adsorption branch.
[d] Determined from the (111) reflection of Cu in the XRD patterns.
[e] Cu dispersion and the exposed Cu specific surface area calculated by N₂O chemisorption.
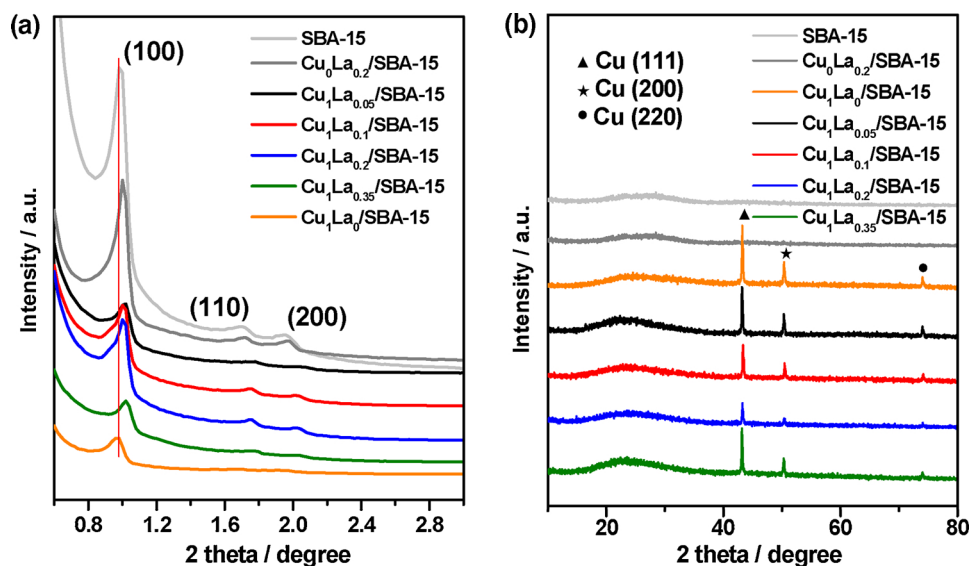[f] Measured by CO₂ Chemisorption.

Fig. 1. (a) Small-angle and (b) large-angle XRD patterns of SBA-15 and reduced Cu₁Laₓ/SBA-15 catalysts.

samples, the specific surface area (347.6–475.3 m²/g) and total pore volume (0.52–0.59 cm³/g) slightly increased compared with Cu₁La₀/SBA-15, but the values were still smaller than those of pristine SBA-15.

The small-angle XRD patterns (Fig. 1a) of as-reduced Cu₁Laₓ/SBA-15 catalysts and pristine SBA-15 showed one major diffraction peak at $2\theta = 0.9°$ for the (100) planes and two other diffraction peaks at $2\theta = 1.7°$ and $2.0°$ for (110) and (200) planes, respectively. These peaks confirmed a well-retained mesostructural order of SBA-15 (P6mm hexagonal symmetry). With the addition of La, the characteristic (100) peak at $0.9°$ slightly shifted to $1.0°$ and exhibited attenuation in intensity. The shift in the characteristic peak to a large angle suggested a slight decrease in the unit cell parameter of SBA-15, reflecting an increase in the thickness of the SBA-15 framework wall. The wide-angle XRD patterns of as-reduced catalysts are displayed in Fig. 1b. Interestingly, no diffraction peaks of La oxides were found in any of the samples, which was possibly because the La species were dispersed well in Cu₁Laₓ/SBA-15 samples. According to the ICP results (Table S1), the La loadings of Cu₁Laₓ/SBA-15 ranged from 0.7 wt% to 6.5 wt%, and the Cu loadings were maintained at approximately 8 wt%. The broad diffraction peak at $2\theta = 23.1°$, which was observed in the diffraction patterns of all catalysts, was assigned to the silica support. Except for the Cu₀La₀.₂/SBA-15, all the catalysts exhibited three diffraction peaks at $2\theta = 43.3°$, $50.4°$, and $74.1°$, which were indexed to the (111), (200), and (220) characteristic facets of metallic Cu, respectively. In addition, the intensity of the metallic Cu diffraction peak declined markedly with

the introduction of La species. The average size of the Cu NPs ($D_{crystallite}$) was estimated from the Scherrer equation using the full-width at half-maximum value of the (111) peak and the minimum $D_{crystallite}$ was 3.8 nm for Cu₁La₀.₂/SBA-15 (Table 1). The above results implied that La and Cu were embedded into the nanochannels, and dispersion on the surface caused some degradation of mesostructures. Furthermore, the results clearly demonstrated that the incorporation of a suitable amount of La hindered the growth of Cu particle size during calcination and reduction. A similar trend determined by dissociative N₂O adsorption was also found. As a result in Table 1, Cu supported on La-modified SBA-15 exhibited higher Cu exposed surface area and dispersion values than the La-free catalysts.

The morphologies and structural details of as-reduced catalysts were examined by TEM (Figure S3). The typical cylindrical and straight channels of SBA-15 were clearly observed over all catalysts. The findings were in agreement with the above N₂ adsorption–desorption isotherm analysis and indicated that the SBA-15 mesoporous structure was not damaged during the catalyst preparation with high-temperature calcination and reduction. Moreover, the images in Figure S3 also indicated that, in the La-free sample, randomly distributed Cu bulks with irregular shape were observed on the external surface of the support. Increasing La amount helped disperse Cu NPs in the pore channels. The nature of La species was considered to affect the particle formation of Cu species when Cu²⁺ ions attracted the deposits on the La species surface during the impregnation process (Scheme 1). The successful
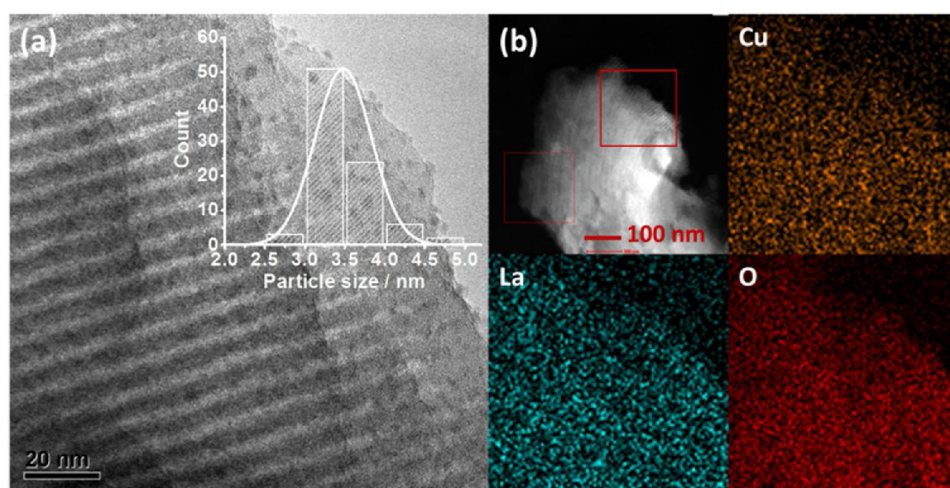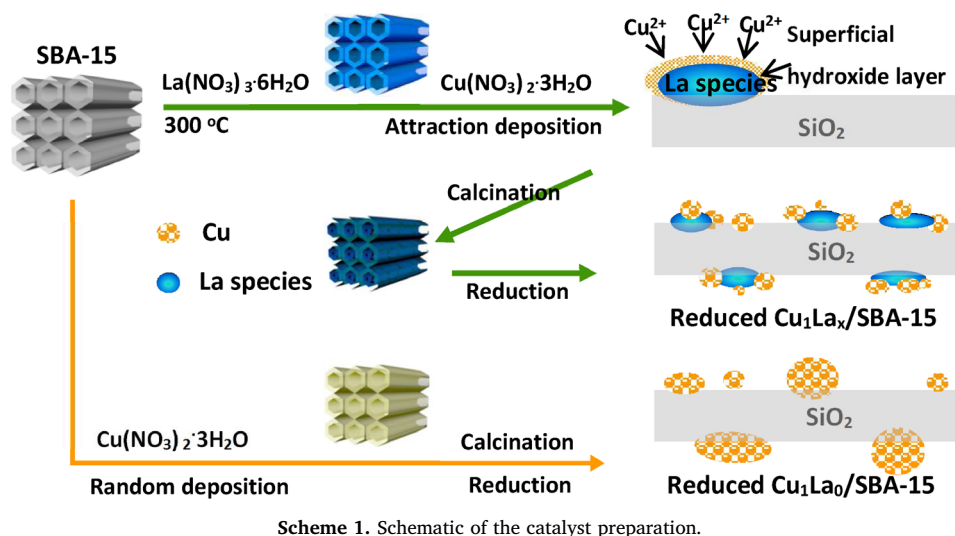
Scheme 1. Schematic of the catalyst preparation.

Fig. 2. (a) TEM image and (b) HAADF-STEM image and EDS elemental mappings of reduced $Cu_1La_{0.2}$/SBA-15 catalyst.

incorporation of the Cu NPs and their particle-size distribution were additionally confirmed by HRTEM analysis. The average diameter of Cu NPs for Cu_1La_0/SBA-15 was around 15.5 $\pm$ 0.5 nm in Figure S4, and it decreased to 3.5 $\pm$ 0.25 nm with the introduction of La species for $Cu_1La_{0.2}$/SBA-15. Furthermore, Fig. 2a again shows that small, uniform Cu NPs were embedded within the pore wall, and the unfilled pore structure of SBA-15 remained. These findings were consistent with the results derived from XRD and N_2O chemisorption analyses discussed earlier. HAADF-STEM characterization and additional EDS mapping on $Cu_1La_{0.2}$/SBA-15 confirmed that Cu, La, and O were evenly dispersed throughout the material (Figs. 2b, S5 and S6).

3.2. Role of La species

Detailed information was obtained regarding the local structure of Cu/La/O species on SiO_2 support. Solid-state ^{29}Si MAS NMR (Fig. 3a) was used to probe the unit structure of SBA-15 and supported catalysts. For such samples, three main peaks were observed at a chemical shift between -120 and -90 ppm. The regions for the Qn sites consisted of Q4 (-112 ppm, $Si(OSi)_4$), Q3 (-104 ppm, $Si(OH)(OSi)_3$), and Q2 (-92 ppm, $Si(OH)_2(OSi)_2$) [47]. The assessment of the influence of SiO_2 support after loading Cu/La/O species could be estimated from the integrated intensities of Qn NMR signals (Table S2). Compared with the Cu_1La_0/SBA-15 and $Cu_1La_{0.2}$/SBA-15 samples, the enhancement in intensity of Q2 and Q3 was clearly visible, which indicated that the

introduction of La species weakened the Si–O–Si interaction in the Si–O tetrahedral structure, resulting in structural defects.

Additionally, XPS experiments were carried out to identify elements from the topmost layers of 3–5 nm-thick slabs of the surface species. The survey spectra are displayed in Fig. 3b. The distinct C 1s and O 1s peaks were observed over La-modified samples, whereas signals corresponding to Cu 2p and La 2p states were weak. As the La content increased, less Cu was enriched on surfaces. To further localize the Cu/La/O species, we performed HS-LEIS studies, which were proven powerful in distinguishing the first layer from the subsurface layers [48,49]. In this experiment, the He^+ ions (weak energy loss) identified almost all elements with poor sensitivity for heavy elements (Cu and La), whereas the Ne^+ ions (strong energy loss) provided better sensitivities for heavy elements and each sputtering depth reached 0.35 nm. Figure S7 shows that almost no Cu/La signal was initially observed from the He^+ spectrum for $Cu_1La_{0.2}$/SBA-15, but a signal appeared after extending the Ne^+ ions sputtering time to clear up silica shell. This result implied that the Cu/La/O species were confined in the SBA-15 mesopores. The changes in Cu/La composition (Fig. 3c) with depth over $Cu_1La_{0.2}$/SBA-15 were tracked using the Ne^+ spectra. The intensity of the Cu signal increased and that of the La signal decreased gradually with increasing sputtering time. The HS-LEIS results provided further evidence that La species was embedded in the pore wall subsurface/surface of SBA-15, and ultra-small Cu NPs were deposited on La species to confine the Cu–LaO_x interface in mesoporous channels.
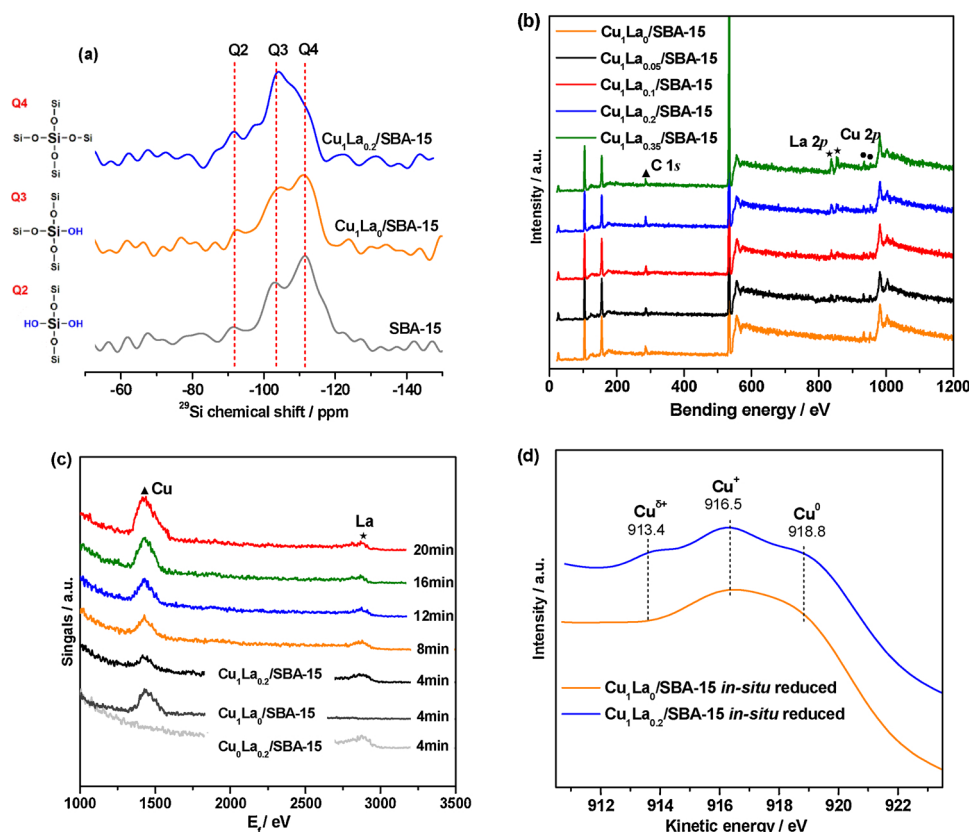
Fig. 3. (a) ^{29}Si MAS NMR of SBA-15 and reduced Cu$_1$La$_x$/SBA-15 catalysts, (b) XPS survey spectra and (c) HS-LEIS spectra of as-reduced Cu$_1$La$_x$/SBA-15 catalysts at 5 keV ^{20}Ne$^+$, and (d) Cu Auger peaks of as-reduced Cu$_1$La$_x$/SBA-15 catalysts.
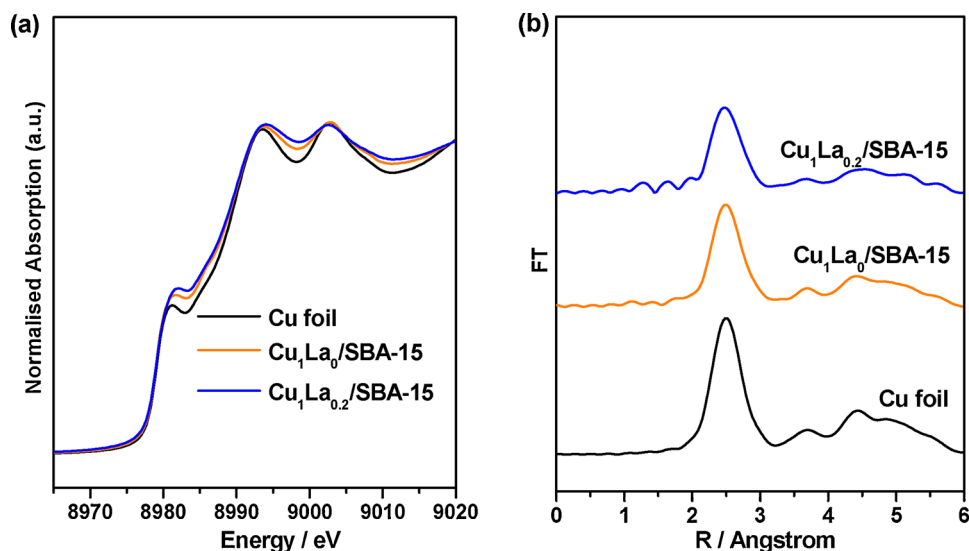

Fig. 4. (a) Normalized Cu K-edge XANES spectra and (b) Fourier transforms of EXAFS oscillation of Cu foil and as-reduced Cu$_1$La$_x$/SBA-15 catalysts.

3.3. Chemical state of Cu species

Usually, supported Cu oxides could not be totally reduced to metallic state (Cu°) under 300 °C and the species of Cu°, Cu$^+$, and even Cu$^{\delta+}$ (not Cu°, Cu$^+$, and Cu^{2+}) may coexist on the reduced catalyst surfaces [50–52]. Here, XAES measurements were conducted to examine the structure of Cu species. The Cu Auger profiles for the supported Cu catalysts with and without La after treatment in 5% H$_2$–95% N$_2$ are shown in Figure S8 and the detailed fitting results are summarized in Table S3. The positions of all Auger peaks were aligned by

the C 1s peak. After in situ reduction, Cu$_1$La$_0$/SBA-15 and Cu$_1$La$_{0.2}$/SBA-15 samples both display two peaks at 916.5 eV and 918.8 eV in Fig. 3d, corresponding to Cu$^+$ and Cu°, respectively [53]. In the Cu Auger spectrum of Cu$_1$La$_{0.2}$/SBA-15 catalyst, a shoulder feature appeared at a kinetic energy of 913.4 eV and became pronounced with the increase of La doping. When the supported pure Cu catalyst was reduced under the same conditions, almost no Auger peak at 913.4 eV was observed. According to the reports in literature [54], the changes in shoulder feature of Cu Auger peak may originate from Cu$^{\delta+}$ in the Cu–LaO$_x$ interface. A similar observation has been reported in previous

work [55], indicating that a slight charge transfer from metal to La was taken place and therefore the electronic effect of $M^{\delta+}$ was added to the geometric effect produced by La^{3+}. Further progression of this effect under more aggressive calcination conditions may lead to the formation of perovskite-type La_2CuO_4, as discussed by several groups [40,54]. For the present catalysts, the content of $Cu^{\delta+}$ species were increased with the increase of La content, supporting the opinion that there exists a strong metal support interaction between the Cu and La species.

We attempted to obtain detailed information regarding the local coordination of the Cu species using XAS. Given that the elemental states and structure of the catalyst might be changed when exposed to air, we carried out these analyses in the absence of air using a special holder with a gas cell to transfer the sample from an inert gas environment to the inside of the instrument. Fig. 4a shows the Cu K-edge XANES spectra for the as-prepared Cu catalysts. Cu foil was used as the standard reference sample. For the Cu_1La_0/SBA-15 and $Cu_1La_{0.2}$/SBA-15 catalysts, even though the XANES spectra were similar to that of Cu foil, the slope of edge absorption was relatively reduced. The Cu K-edge EXAFS $K^3\chi(R)$ functions and their Fourier transform (FT) are shown in Fig. 4b. One small peak of the $Cu_1La_{0.2}$/SBA-15 sample at 1.84 Å was from the Cu−O contribution, and the other strong peak at 2.54 Å was from the Cu−Cu subshell contribution referring to the standard sample. Table 2 shows the local coordination structure of Cu species estimated by EXAFS curve-fitting for the prepared samples. The Cu−O shell was observed over the $Cu_1La_{0.2}$/SBA-15 sample with coordination number of 0.4 at a bond distance of 1.84 ± 0.03 Å. Furthermore, with the introduction of La, the coordination number of the Cu−Cu shell from 9.3 ± 0.6 changed to 7.7 ± 0.2, indicating that the Cu−Cu bond was partly replaced by O to form Cu−O−La bond. These measurements demonstrated the importance of La in affecting the local environment of Cu species in Cu-based catalysts.

3.4. Reducibility and CO₂–TPD of Cu₁Laₓ/SBA-15

The reduction behavior of the calcined Cu_1La_x/SBA-15 samples was investigated by H_2-TPR and the corresponding reduction profiles are given in Fig. 5a. All samples showed a broad reduction peak between 225 °C and 375 °C, which could be attributed to the reduction of Cu oxide. For the Cu_1La_0/SBA-15 sample, a reduction peak existed at less than 320 °C which was probably because the majority of CuO species were present on the outside of the mesoporous silica surface and easily reduced. In comparison with the unmodified sample, the maximum strength of reduction over Cu_1La_x/SBA-15 samples shifted from 308 °C to 351 °C due to the introduction of La before Cu loading. The peak shift suggested that the interaction between Cu and La species considerably helped resisting the sintering of Cu NPs during the calcination and reduction.

One of the promotional effects of La was improved Cu dispersion to maximize the number of exposed Cu−LaOₓ interface as discussed above. In addition, the basicity of Cu/La/O species was expected to increase adsorption/activation of mildly acidic CO_2 in previous studies [56]. In Table 1, the total CO_2 uptake amounts for Cu_1La_x/SBA-15 catalysts follow the order of Cu_1La_0/SBA-15 (36.1 μmol/g) < $Cu_1La_{0.05}$/SBA-15 (54.7 μmol/g) < $Cu_1La_{0.1}$/SBA-15 (72.9 μmol/g) < $Cu_1La_{0.2}$/SBA-15 (151.3 μmol/g) < $Cu_1La_{0.35}$/SBA-15 (160.4 μmol/g). Subsequently, CO_2–TPD was used to study the desorption behavior of

CO_2 from the active sites on the Cu_1La_x/SBA-15 catalysts, and the results are shown in Fig. 5b. Under the same experimental conditions, the pure Cu-supported catalyst barely showed CO_2 adsorption; however, a peak associated with CO_2 desorption appeared (< 150 °C) upon $Cu_1La_{0.05}$/SBA-15 and another new desorption peak (at 200–300 °C) was observed over $Cu_1La_{0.1}$/SBA-15. As the La/Cu atomic ratio increased from 0.05 to 0.35, the intensity of desorption peak was markedly enhanced, especially at high temperatures. The desorption peak above 500 °C was assignable to the decomposition of lanthanum carbonate species, in other words, lanthanum carbonate species can be formed, particularly in the case of La/Cu atomic ratio higher than 0.05. Nevertheless, CO_2 was desorbed from $Cu_1La_{0.2}$/SBA-15 and the relative intensities for moderately basic sites were greater than those from the other Cu_1La_x/SBA-15 catalysts. Considering the moderately CO_2 chemical desorption at 200–300 °C, we speculated that this part of CO_2 might be activated and hydrogenated in the next step without producing lanthanum carbonate species which require higher temperature to decompose.

3.5. CO₂ hydrogenation

It is well known that Cu–oxide interfaces, such as Cu–ZnO [57] or Cu–ZrO_2 [58], are commonly proposed to play a key role in the selective formation of methanol. Prior to examining the CO_2 hydrogenation facilitated by Cu–LaOₓ interface dispersed on mesopores silicas, control experiments were performed to understand the role of each composition in catalysis. The catalytic activity tests for as-prepared catalyst were conducted using a high-pressure fixed-bed flow reactor. As shown in Table S4, the Cu free catalyst showed almost no activity for CO_2 hydrogenation because the La species or SiO_2 was short of catalytically active sites for cracking hydrogen, which is the first fundamental step of hydrogenation. The Cu_1La_0/SBA-15 catalyst exhibited low hydrogenation activity with only 26.2% selectivity for methanol. Considering that the RWGS was highly favorable compared with methanol formation on conventional undistorted pure Cu surface, CO should almost always be one of dominant products [59]. Increased activity for methanol formation was achieved on $Cu_1La_{0.2}$/SBA-15. In order to further clarify the effects of Cu–LaOₓ interface, a Cu@LaOₓ catalyst was fabricated by depositing La species layer onto the surface of commercial Cu microparticles (MPs). SEM images revealed that the deposition was successful (Figure S9). The measured BET surface area of this catalyst (23.1 m²/g) was higher than Cu MPs (11.2 m²/g).

Fig. 6a shows the measured TOF and methanol production over the commercial Cu MPs and Cu@LaOₓ as a function of temperature. It can be seen that Cu coated with La species stands out as being particularly active towards methanol synthesis. The methanol production rate was over 13 times higher than on uncoated Cu MPs at the reaction temperature between 220 °C and 280 °C. The TOF, which represents the number of CO_2 molecules hydrogenated on the unit site of an exposed Cu atom per hour (h^{-1}), was calculated from the exposed Cu surface area for various catalysts. The results from this study showed that the TOF increased more than 5 times over Cu@LaOₓ in comparison with uncoated Cu MPs at 240 °C. Moreover, the E_a over Cu@LaOₓ was measured to be 62.5 kJ/mol (Fig. 6b), lower than that on Cu MPs (96.6 kJ/mol). These results indicated that the as-built Cu–LaOₓ interface would facilitate CO_2 hydrogenation to methanol.

Table 2
Curve fitting results of Cu K-edge EXAFS for different samples.

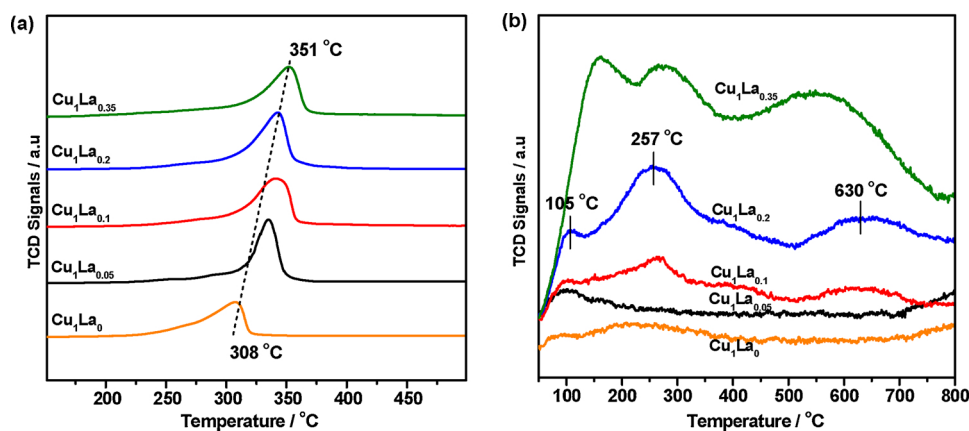| Sample	Scattering path	Radial distance (Å)	Coordination number	Debye-Waller factor	Energy difference (eV)
Cu foil	Cu–Cu	2.54 ± 0.01	12 ± 0.6	0.009 ± 0.001	3.0
Cu_1La_0/SBA-15	Cu–Cu	2.54 ± 0.01	9.3 ± 0.6	0.009 ± 0.001	4.1
$Cu_1La_{0.2}$/SBA-15	Cu–O	1.84 ± 0.03	0.4 ± 0.1	0.004 ± 0.001	4.2
	Cu–Cu	2.54 ± 0.01	7.7 ± 0.2	0.008 ± 0.001	

Fig. 5. (a) H_2–TPR profile of as-calcined Cu_1La_x/SBA-15 and (b) CO_2–TPD profile of as-reduced Cu_1La_x/SBA-15 catalysts.

As the promotional effect induced by the Cu–LaO_x interface, creating more Cu–LaO_x interfaces should lead to further enhanced catalytic efficiency. Confined Cu/La/O species in porous SiO_2, where abundant Cu–LaO_x interface was created, was expected to boost the hydrogenation. Thus, Cu_1La_x/SBA-15 catalysts were synthesized, where highly-dispersed Cu–LaO_x interface was generated through the interaction of Cu NPs with La species bedded into the SBA-15 pore wall. Fig. 7a shows the product selectivity versus the TOF on Cu_1La_x/SBA-15 catalysts. We noted that the activity for CO_2 hydrogenation was greatly enhanced, suggesting that introducing La into Cu–SiO_2 had a promotional effect on catalytic performance. In general, increasing the La loading increased TOF and methanol selectivity. By contrast, CO selectivity decreased with increasing La loading. Among all samples, the $Cu_1La_{0.2}$/SBA-15 catalyst exhibited the highest catalytic activity (TOF up to $20.4\,h^{-1}$) with 81.2% methanol selectivity. The methanol formation rate was determined to be 190.8 mg/g_{-cat}·h, which was about 10 times greater than Cu alone supported Cu_1La_0/SBA-15 catalyst (19.8 mg/g_{-cat}·h), and compared favorably with other reported Cu-based catalysts (Table S4). This remarkable enhancement clearly demonstrated that the Cu–LaO_x interface was suitable for CO_2 hydrogenation to methanol. Fig. 7b compares the CO_2 conversion with the methanol formation rate on Cu_1La_0/SBA-15 and $Cu_1La_{0.2}$/SBA-15 catalysts as a function of reaction temperature (Table S5). As expected, the $Cu_1La_{0.2}$/SBA-15 catalyst possessed higher rates of CO_2 conversion and methanol formation with increasing reaction temperature from 200 °C to 300 °C. The influences of calcination temperature, reduction

temperature, reaction pressure, and GHSV on CO_2 hydrogenation performance over $Cu_1La_{0.2}$/SBA-15 are successively presented in Figures S10 and S11. When the calcination temperature was increased, both CO_2 conversion and methanol selectivity were increased but the CO selectivity was decreased. The results indicated that higher calcination temperature might significantly enhance the Cu–LaO_x interactions. When the reduction temperature was set higher than 400 °C, both CO_2 conversion and methanol selectivity were rapidly decreased. Thus, the $Cu_1La_{0.2}$/SBA-15 catalyst reduced around 300 °C could be expected to exhibit excellent performance and stability. Higher pressure and GHSV were beneficial to the methanol yield. When the reaction pressure was increased to 5.0 MPa, the methanol yield reached as high as 243.6 mg/g_{-cat}·h with a CO_2 conversion of 6.9% at 240 °C.

3.6. Catalyst stability

The stability of Cu_1La_x/SBA-15 catalysts is also an important parameter to consider for a Cu-based supported catalyst. The susceptibility of these catalysts to undergo Cu sintering and interface separation is often responsible for their limited industrial applications. The performances of the Cu_1La_0/SBA-15 and $Cu_1La_{0.2}$/SBA-15 catalysts were monitored for an extended amount of time. The results of this study are shown in Fig. 8. A rapid drop in the catalytic activity of Cu_1La_0/SBA-15 was observed after 24 h, which indicated poor stability. However, little deactivation was observed over the $Cu_1La_{0.2}$/SBA-15 catalyst after 100 h of evaluation. The conversion of CO_2 remained at 6%, and
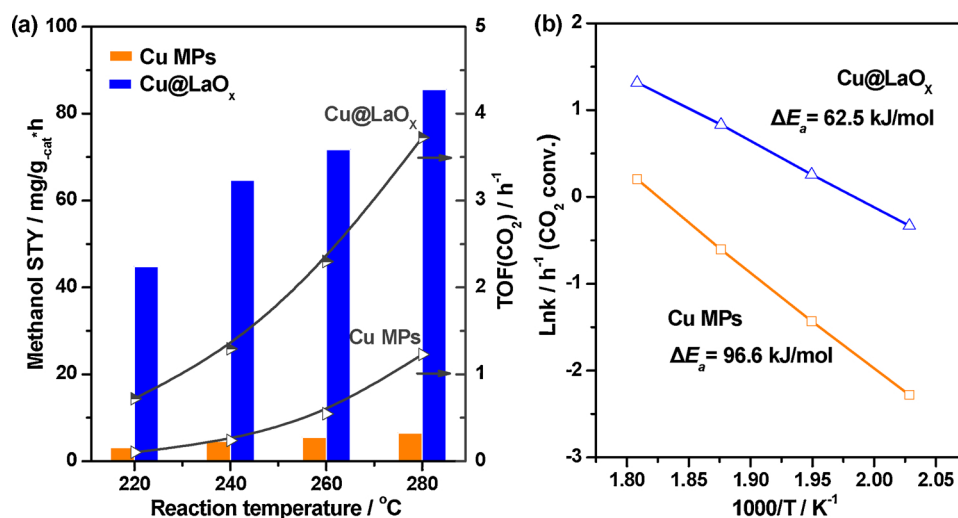

Fig. 6. (a) Catalytic performance and (b) E_a of Cu MPs before and after coating La species for CO_2 hydrogenation. Reaction conditions: 240 °C, 3.0 MPa, H_2:CO_2:N_2 = 72:24:4, and GHSV = 12,000 mL/g_{-cat}·h.
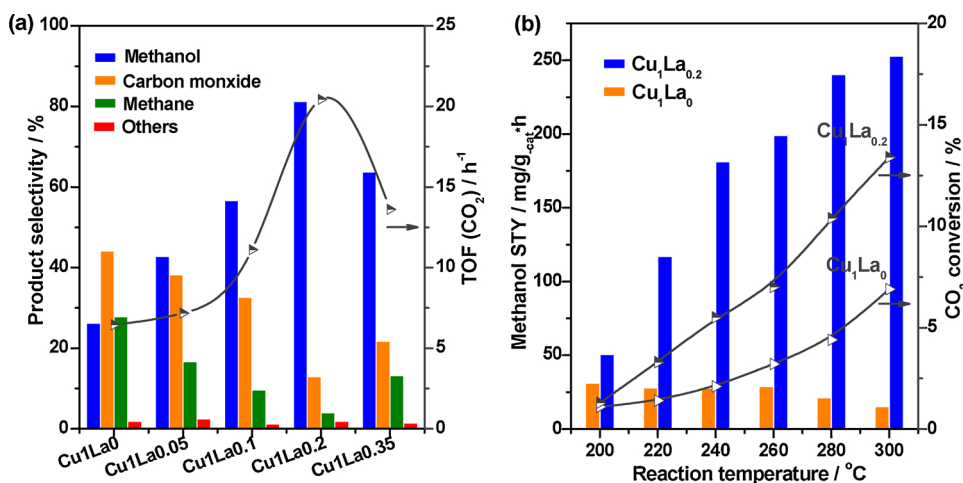
Fig. 7. (a) CO_2 hydrogenation performance of Cu_1La_x/SBA-15 catalysts at 240 °C as a function of Cu/La atomic ratio. (b) Methanol space time yield and CO_2 conversion over Cu_1La_0/SBA-15 and $Cu_1La_{0.2}$/SBA-15 catalysts as a function of reaction temperature. Reaction conditions: 240 °C, 3.0 MPa, H_2:CO_2:N_2 = 72:24:4, and GHSV = 12,000 mL/g_{-cat}·h.
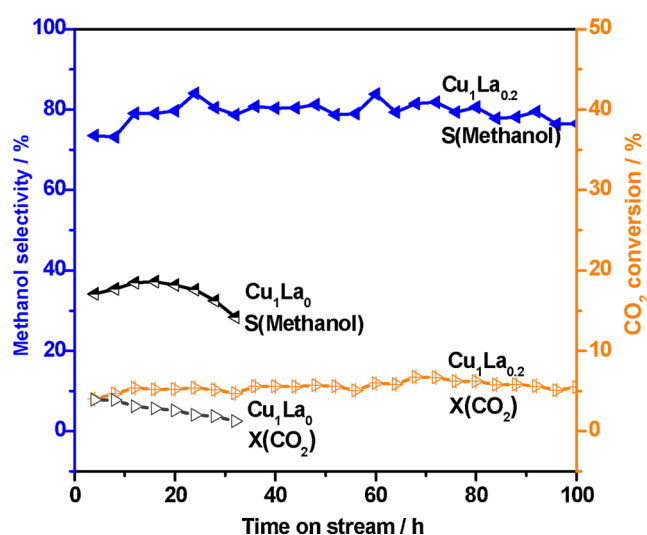

Fig. 8. Evolution of methanol selectivity and CO_2 conversion with time on stream over Cu_1La_0/SBA-15 and $Cu_1La_{0.2}$/SBA-15 catalysts. Reaction conditions: 240 °C, 3.0 MPa, H_2:CO_2:N_2 = 72:24:4, and GHSV = 12,000 mL/g_{-cat}·h.

methanol selectivity did not drop and remained at about 80%, indicating that the $Cu_1La_{0.2}$/SBA-15 catalyst showed long-term stability for selectively hydrogenating CO_2 to methanol.

3.7. Proposed reaction mechanism over the Cu–LaO_x interfaces

A question we can raise by the above results is why the methanol synthesis activity of La-modified Cu catalyst is higher than for the La-free counterpart. Apparently, there are two factors that affect the synthesis rate, i. e., the type of metal-oxide interfaces and the number of metal-oxide interfacial area. At the Cu–LaO_x interface, the adsorption and dissociation of H_2 occur on the Cu sites, while the adsorption of CO_2 takes place over the La sites. The atomic-hydrogen transfers to La sites via spillover and hydrogenates the adsorbed carbon-containing species to form methanol. It is different for the undistorted pure Cu surfaces, where both RWGS and methanol synthesis proceed at the same surface site. Because CO does not bind strongly enough to Cu, easily decomposed phenomenon will be observed, which translates into a higher RWGS activity and hence lower methanol selectivity.

A more detailed analysis supporting this argument can be verified by H/D exchange experiments. The kinetic isotope effect for methanol synthesis of $Cu_1La_{0.2}$/SBA-15 catalyst (k_H/k_D = 0.82) was about two times lower than for CO formation (k_H/k_D = 1.59) at 240 °C revealed that the isotope effects was stronger for methanol synthesis than for

RWGS on Cu–LaO_x interface. The temperature variation study of Fig. 7b was repeated with a CO_2:H_2/D_2 feed (1:3) as shown in Figure S12. The methanol formation rates showed a significant raise in CO_2/D_2 feed at different reaction temperatures. Figure S13 illustrates how H/D substitution affects the methanol selectivity of pure Cu and Cu–LaO_x interface at 240 °C. When CO_2 hydrogenated in D_2, about 5% of the increase (up to 85%) in methanol selectivity was observed over the Cu@LaO_x and $Cu_1La_{0.2}$/SBA-15 catalysts. When D_2 was switched to H_2, the methanol selectivity returned to the original values (80%). Interestingly, an opposite trend was observed when D_2 was introduced into the reaction stream, methanol selectivity dropped from 38.4% to 18.5% for the Cu MPs catalysts, but once again the selectivity returned within 60 min when the D_2 was switched to H_2. This reverse variation between Cu MPs and Cu@LaO_x was consistent with the preceding observation that different active surface sites were responsible for each reaction and did not share a common intermediate. In situ DRIFTS experiments were performed to identify the key intermediates during CO_2 hydrogenation over Cu_1La_0/SBA-15 and $Cu_1La_{0.2}$/SBA-15 catalysts. Fig. 9a shows the evolution of the principal surface species with increasing CO_2 hydrogenation reaction pressure at 240 °C. HCOO* and H_3CO* species were observed and identified. The peaks at 1348 and 1597 cm^{-1} were assigned to the O−C−O stretching vibrations of adsorbed bidentate HCOO* species. The peaks at 2764 and 2892 cm^{-1} were assigned to the C−H stretch vibration in the *HCOO species. The peaks at 1048, 1464, 2819, 2846, and 2926 cm^{-1} were attributed to the H_3CO* species [60–64]. The peaks at 2892 and 2846 cm^{-1} were used to follow the concentration changes in *HCOO and *H_3CO species, respectively. For the CO_2 + H_2 reaction at atmospheric pressure over $Cu_1La_{0.2}$/SBA-15, the surface bidentate *HCOO species were generated. Furthermore, the intensity of the *H_3CO species at 2926 cm^{-1} became apparent after the reaction pressure was increased to 5 bar. It continued to increase but reached a stable value after 30 min at 10 bar. The surface bidentate *HCOO species on Cu_1La_0/SBA-15 increased gradually with increasing reaction pressure, whereas the *H_3CO species on Cu_1La_0/SBA-15 was barely visible until 10 bar. On the basis of the peak intensity of the vibrational bands *HCOO and *H_3CO species on $Cu_1La_{0.2}$/SBA-15 were more visible than those on Cu_1La_0/SBA-15, indicating that $Cu_1La_{0.2}$/SBA-15 was more effective than Cu_1La_0/SBA-15 in CO_2 activation and CH_3OH formation.

To trace the evolution of hydrogenated intermediates, the key surface species formed from CO_2 + H_2 at atmospheric pressure were recorded over $Cu_1La_{0.2}$/SBA-15. When the reaction gas phase of CO_2 + H_2 was switched to pure D_2, the peaks at 2892 and 2846 cm^{-1} of the HCOO* and H_3CO* species, respectively, declined rapidly and disappeared after 30 min (Figs. 9b). Correspondingly, two new peaks at 2221 and 2068 cm^{-1} due to the H/D exchanged DCOO* and HD_2CO* intermediate species, respectively, appeared, grew, and disappeared
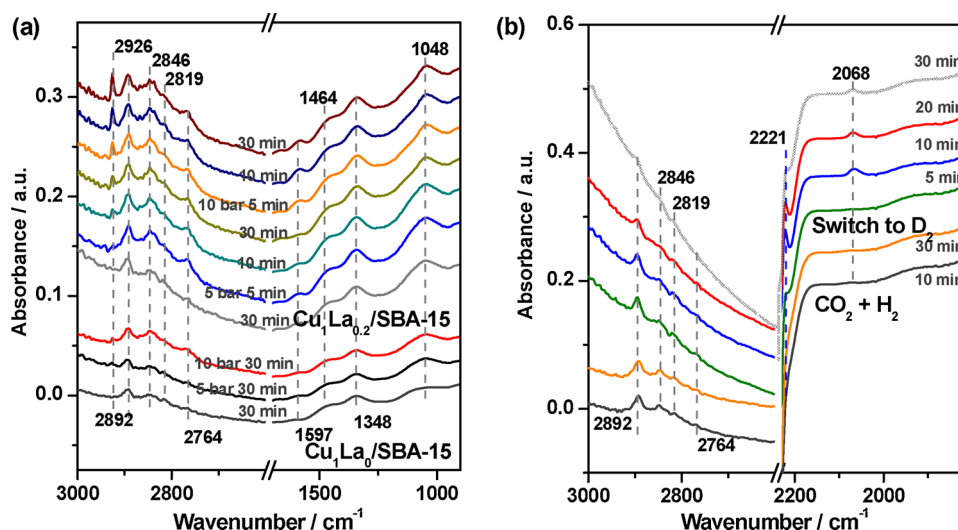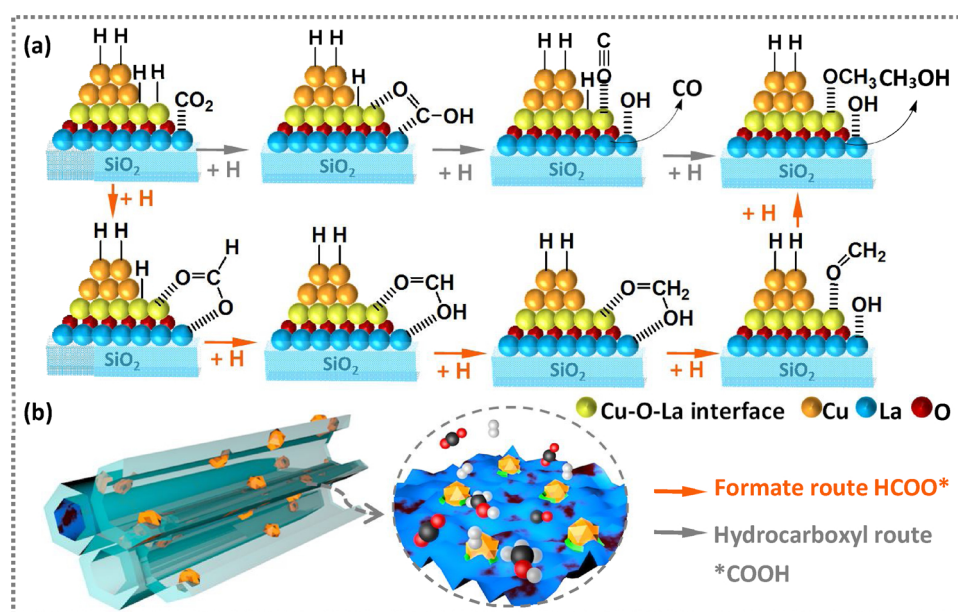
Fig. 9. (a) In situ DRIFTS of CO_2 + H_2 reaction over Cu_1La_0/SBA-15 and $Cu_1La_{0.2}$/SBA-15 catalysts. (b) In situ DRIFTS of CO_2 + H_2 reaction and then switching CO_2 + H_2 to pure D_2 over $Cu_1La_{0.2}$/SBA-15 catalyst. Reaction conditions: 300 °C, 5%H_2–N_2, in-situ reduction 1 h, 240 °C, 0.1 MPa, H_2:CO_2:N_2 = 72:24:4, and 20 mL/min.

Scheme 2. Proposed reaction mechanism for CO_2 hydrogenation over $Cu_1La_{0.2}$/SBA-15 catalyst.

slowly. These changes reflected the dynamic process of surface HCOO* hydrogenated to H_3CO* over $Cu_1La_{0.2}$/SBA-15 catalyst. In general, two major reactions pathways have been proposed for CO_2 hydrogenation to methanol on the basis of previous experimental observations and theoretical calculations [65–68]. The first pathway was produced from the carboxylate (*COOH) route and bound through a single O atom or along the formate pathway, adsorbed through two O atoms in the bidentate configuration (*HCOO), and further hydrogenated to the final product CH_3OH (Scheme 2). DRIFTS experiments demonstrated that the formate (HCOO*) route was preferable in methanol formation at the Cu–LaO_x interface.

4. Conclusions

In summary, a class of stable supported Cu catalysts with substantial Cu–LaO_x interface has been developed for the CO_2 hydrogenation to methanol. The best catalytic performance is achieved with $Cu_1La_{0.2}$/SBA-15 catalyst, which outperforms La-free counterpart, exhibiting greatly enhanced catalytic activity and stability. The effective synthesis

of methanol results from three factors. (1) Cu species are delivered into La-modified SBA-15 mesopores which are considerably beneficial for the sintering-resistance of Cu NPs; (2) The Cu–LaO_x interface possesses excellent adsorption capacity of acidic CO_2; (3) At the Cu–LaO_x interface, the formate (HCOO*) route is preferable for the methanol production than that of CO_2 reduction to *COOH first and then decomposition of *COOH to CO. The findings highlight the importance of the metal–oxide interfaces and shed some lights on rational design of stable and effective catalysts for CO_2 hydrogenation.

Acknowledgements

Engineering (2016-13).

Appendix A. Supplementary data

Supplementary material related to this article can be found, in the online version, at doi:https://doi.org/10.1016/j.apcatb.2019.03.059.

References

[1] M. Aresta, Carbon Dioxide As Chemical Feedstock, John Wiley & Sons, 2010.
[2] B.A. Pinaud, J.D. Benck, L.C. Seitz, A.J. Forman, Z.B. Chen, T.G. Deutsch, B.D. James, K.N. Baum, G.N. Baum, S. Ardo, H.L. Wang, E. Miller, T.F. Jaramillo, Energy Environ. Sci. 6 (2013) 1983–2002.
[3] M.E. Boot-Handford, J.C. Abanades, E.J. Anthony, M.J. Blunt, S. Brandani, N. Mac Dowell, J.R. Fernández, M.C. Ferrari, R. Gross, J.P. Hallett, R.S. Haszeldine, P. Heptonstall, A. Lyngfelt, Z. Makuch, E. Mangano, R.T.J. Porter, M. Pourkashanian, G.T. Rochelle, N. Shah, J.G. Yao, P.S. Fennell, Energy Environ. Sci. 7 (2014) 130–189.
[4] G. Centi, S. Perathoner, Catal. Today 148 (2009) 191–205.
[5] H. Wang, P. Gao, T.J. Zhao, W. Wei, Y.H. Sun, Sci. China Chem. 58 (2015) 79–92.
[6] G.A. Olah, Angew. Chem. Int. Ed. 44 (2005) 2636–2639.
[7] A. Goeppert, M. Czaun, J.-P. Jones, G.K.S. Prakash, G.A. Olah, Chem. Soc. Rev. 43 (2014) 7995–8048.
[8] M.D. Porosoff, B. Yan, J.G.G. Chen, Energy Environ. Sci. 9 (2016) 62–73.
[9] M. Behrens, F. Studt, I. Kasatkin, S. Kühl, M. Hävecker, F. Abild-Pedersen, S. Zander, F. Girgsdies, P. Kurr, B.-L. Kniep, M. Tovar, R.W. Fischer, J.K. Nørskov, R. Schlögl, Science 336 (2012) 893–897.
[10] V. Schott, H. Oberhofer, A. Birkner, M.C. Xu, Y.M. Wang, M. Muhler, K. Reuter, C. Wöell, Angew. Chem. Int. Ed. 52 (2013) 11925–11929.
[11] S. Kuld, M. Thorhauge, H. Falsig, C.F. Elkjaer, S. Helveg, I. Chorkendorff, J. Sehested, Science 352 (2016) 969–974.
[12] S. Kattel, P.J. Ramirez, J.G.G. Chen, J.A. Rodriguez, P. Liu, Science 355 (2017) 1296–1299.
[13] M.B. Fichtl, D. Schlereth, N. Jacobsen, I. Kasatkin, J. Schumann, M. Behrens, R. Schlögl, O. Hinrichsen, Appl. Catal. A: Gen. 502 (2015) 262–270.
[14] B. An, J.Z. Zhang, K. Cheng, P.F. Ji, C. Wang, W.B. Lin, J. Am. Chem. Soc. 139 (2017) 3834–3840.
[15] B. Zhang, Y. Chen, J.W. Li, E. Pippel, H.M. Yang, Z. Gao, Y. Qin, ACS Catal. 5 (2015) 5567–5573.
[16] L.R. Winter, E. Gomez, B.H. Yan, S.Y. Yao, J.G. Chen, Appl. Catal. B: Environ. 224 (2018) 442–450.
[17] C.F. Xu, G.X. Chen, Y. Zhao, P. Liu, X.P. Duan, L. Gu, G. Fu, Y.Z. Yuan, N.F. Zheng, Nat. Commun. 9 (2018) 3367–3377.
[18] M. Romero-Sáez, A.B. Dongil, N. Benito, R. Espinoza-González, N. Escalona, F. Gracia, Appl. Catal. B: Environ. 237 (2018) 817–825.
[19] W.Y. Zhang, Q. Qin, L. Dai, R.X. Qin, X.J. Zhao, X.M. Chen, D.H. Ou, J. Chen, T.T. Chuong, B.H. Wu, N.F. Zheng, Angew. Chem. Int. Ed. 57 (2018) 9475–9479.
[20] A. Karelovic, P. Ruiz, Catal. Sci. Technol. 5 (2015) 869–881.
[21] X.S. Dong, F. Li, N. Zhao, F.K. Xiao, J.W. Wang, Y.S. Tan, Appl. Catal. B: Environ. 191 (2016) 8–17.
[22] J.T. Billy, A.C. Co, Appl. Catal. B: Environ. 237 (2018) 911–918.
[23] Q. Zhang, Y.Z. Zuo, M.H. Han, J.F. Wang, Y. Jin, F. Wei, Catal. Today 150 (2010) 55–60.
[24] P. Gao, F. Li, N. Zhao, F.K. Xiao, W. Wei, L.S. Zhong, Y.H. Sun, Appl. Catal. A: Gen. 468 (2013) 442–452.
[25] P. Gao, L.S. Zhong, L.N. Zhang, H. Wang, N. Zhao, W. Wei, Y.H. Sun, Catal. Sci. Technol. 5 (2015) 4365–4377.
[26] R. Ladera, F.J. Pérez-Alonso, J.M. González-Carballo, M. Ojeda, S. Rojas, J.L.G. Fierro, Appl. Catal. B: Environ. (2013) 142–143 241–248.
[27] P. Gao, F. Li, H.J. Zhan, N. Zhao, F.K. Xiao, W. Wei, L.S. Zhong, H. Wang, Y.H. Sun, J. Catal. 298 (2013) 51–60.
[28] L.X. Zhang, Y.C. Zhang, S.Y. Chen, Appl. Catal. A: Gen. (2012) 415–416 118–123.
[29] H. Ren, C.H. Xu, H.Y. Zhao, Y.X. Wang, J. Liu, J.Y. Liu, J. Ind. Eng. Chem. 28 (2015) 261–267.
[30] J. Graciani, K. Mudiyanselage, F. Xu, A.E. Baber, J. Evans, S.D. Senanayake, D.J. Stacchiola, P. Liu, J. Hrbek, J. Fernandez Sanz, J.A. Rodriguez, Science 345
[31] H.M. Duan, Y.X. Yang, J. Patel, D. Dumbre, S.K. Bhargava, N. Burke, Y.C. Zhai, P.A. Webley, Mater. Res. Bull. 60 (2014) 232–237.
[32] B. Rungtaweevoranit, J. Baek, J.R. Araujo, B.S. Archanjo, K.M. Choi, O.M. Yaghi, G.A. Somorjai, Nano Lett. 16 (2016) 7645–7649.
[33] L. Li, D.S. Mao, J. Yu, X.M. Guo, J. Power Sources 279 (2015) 394–404.
[34] C.L. Zhong, X.M. Guo, D.S. Mao, S. Wang, G.S. Wu, G.Z. Lu, RSC Adv. 5 (2015) 52958–52965.
[35] A. Bansode, B. Tidona, P.R. von Rohr, A. Urakawa, Catal. Sci. Technol. 3 (2013) 767–778.
[36] X.M. Guo, D.S. Mao, G.Z. Lu, S. Wang, G.S. Wu, J. Mol. Catal. A: Chem. 345 (2011) 60–68.
[37] D. Wierzbicki, R. Baran, R. Dębek, M. Motak, M.E. Gálvez, T. Grzybek, P.D. Costa, P. Glatzel, Appl. Catal. B: Environ. 232 (2018) 409–419.
[38] Y.Q. Song, X.R. Liu, L.F. Xiao, W. Wu, J.W. Zhang, X.M. Song, Catal. Lett. 145 (2015) 1272–1280.
[39] L.Y. Mo, K.K.M. Leong, S. Kawi, Catal. Sci. Technol. 4 (2014) 2107–2114.
[40] X.L. Zheng, H.Q. Lin, J.W. Zheng, X.P. Duan, Y.Z. Yuan, ACS Catal. 3 (2013) 2738–2749.
[41] K. Chen, X.P. Duan, H.H. Fang, X.L. Liang, Y.Z. Yuan, Catal. Sci. Technol. 8 (2018) 1062–1069.
[42] J. Dou, Y. Sheng, C. Choong, L.W. Chen, H.C. Zeng, Appl. Catal. B Environ. 219 (2017) 580–591.
[43] A. Atakan, P. Mäkie, F. Söderlind, J. Keraudy, E.M. Björk, M. Odén, Phys. Chem. Chem. Phys. 19 (2017) 19139–19149.
[44] S. Tada, A. Katagiri, K. Kiyota, T. Honma, H. Kamei, A. Nariyuki, S. Uchida, S. Satokawa, J. Phys. Chem. C 122 (2018) 5430–5442.
[45] D.Y. Zhao, J.Y. Sun, Q.Z. Li, G.D. Stucky, Chem. Mater. 12 (2000) 275–279.
[46] A. Gervasini, S. Bennici, Appl. Catal. A: Gen. 281 (2005) 199–205.
[47] C.S. Chen, C.S. Budi, H.C. Wu, D. Saikia, H.M. Kao, ACS Catal. 7 (2017) 8367–8381.
[48] J.W. Zheng, J. Qu, H.Q. Lin, Q. Zhang, X. Yuan, Y.H. Yang, Y.Z. Yuan, ACS Catal. 6 (2016) 6662–6669.
[49] M.M.J. Li, L.M. Ye, J.W. Zheng, H.H. Fang, A. Kroner, Y.Z. Yuan, S.C.E. Tsang, Chem. Commun. 52 (2016) 2569–2572.
[50] H.J. Zhan, F. Li, P. Gao, N. Zhao, F.K. Xiao, W. Wei, L.S. Zhong, Y.H. Sun, J. Power Sources 251 (2014) 113–121.
[51] F. Arena, G. Italiano, K. Barbera, G. Bonura, L. Spadaro, F. Frusteri, Catal. Today 143 (2009) 80–85.
[52] F. Arena, G. Italiano, K. Barbera, S. Bordiga, G. Bonura, L. Spadaro, F. Frusteri, Appl. Catal. A: Gen. 350 (2008) 16–23.
[53] G.Q. Cui, X.Y. Meng, X. Zhang, W.L. Wang, S.L. Xu, Y.C. Ye, K.J. Tang, W.M. Wang, J.H. Zhu, M. Wei, D.G. Evans, X. Duan, Appl. Catal. B: Environ. 248 (2019) 394–404.
[54] H.J. Zhan, F. Li, C.L. Xin, N. Zhao, F.K. Xiao, W. Wei, Y.H. Sun, Catal. Lett. 145 (2015) 1177–1185.
[55] N.S. Figoli, P.C. Largentiere, A. Arcoya, X.L. Seoane, J. Catal. 155 (1995) 95–105.
[56] D. Wierzbicki, R. Baran, R. Dębek, M. Motak, M.E. Gálvez, T. Grzybek, P.D. Costa, P. Glatzel, Appl. Catal. B: Environ. 232 (2018) 409–419.
[57] H. Lei, R.F. Nie, G.Q. Wu, Z.Y. Hou, Fuel 154 (2015) 161–166.
[58] K. Larmier, W.C. Liao, S. Tada, E. Lam, R. Verel, A. Bansode, A. Urakawa, A. Comas-Vives, C. Copéret, Angew. Chem. Int. Ed. 56 (2017) 2318–2323.
[59] Z.Q. Wang, Z.N. Xu, S.Y. Peng, M.J. Zhang, G. Lu, Q.S. Chen, Y.M. Chen, G.C. Guo, ACS Catal. 5 (2015) 4255–4259.
[60] I.A. Fisher, A.T. Bell, J. Catal. 172 (1997) 222–237.
[61] D. Bianchi, T. Chafik, M. Khalfallah, S.J. Teichner, Appl. Catal. A: Gen. 123 (1995) 89–110.
[62] D. Bianchi, T. Chafik, M. Khalfallah, S.J. Teichner, Appl. Catal. A: Gen. 105 (1993) 223–249.
[63] M.D. Rhodes, A.T. Bell, J. Catal. 233 (2005) 198–209.
[64] S. Kattel, B.H. Yan, Y.X. Yang, J.G.G. Chen, P. Liu, J. Am. Chem. Soc. 138 (2016) 12440–12450.
[65] J.J. Wang, G.N. Li, Z.L. Li, C.Z. Tang, Z.C. Feng, H.Y. An, H.L. Liu, T.F. Liu, C. Li, Sci. Adv. 3 (2017) e1701290.
[66] C. Liu, B. Yang, E. Tyo, S. Seifert, J. DeBartolo, B. von Issendorff, P. Zapol, S. Vajda, L.A. Curtiss, J. Am. Chem. Soc. 137 (2015) 8676–8679.
[67] L.C. Grabow, M. Mavrikakis, ACS Catal. 1 (2011) 365–384.
[68] Z.J. Wang, H. Song, H. Pang, Y.X. Ning, T.D. Dao, Z. Wang, H.L. Chen, Y.X. Weng, Q. Fu, T. Nagao, Y.M. Fang, J.H. Ye, Appl. Catal. B: Environ. 250 (2019) 10–16.